# $A$Fe$_2$As$_2$ ($A$ = Ca, Sr, Ba, Eu) and SrFe$_{2-x}$TM$_x$As$_2$ ($TM$ = Mn, Co, Ni): crystal structure, charge doping, magnetism and superconductivity

**Deepa Kasinathan**[1]**, Alim Ormeci, Katrin Koch, Ulrich Burkhardt, Walter Schnelle, Andreas Leithe-Jasper and Helge Rosner**[1]

Max-Planck-Institut für Chemische Physik fester Stoffe, Dresden, Germany
E-mail: Deepa.Kasinathan@cpfs.mpg.de and Rosner@cpfs.mpg.de

**Abstract.** The electronic structure and physical properties of the pnictide compound families $RE$OFeAs ($RE$ = La, Ce, Pr, Nd, Sm), $A$Fe$_2$As$_2$ ($A$ = Ca, Sr, Ba, Eu), LiFeAs and FeSe are quite similar. Here, we focus on the members of the $A$Fe$_2$As$_2$ family whose sample composition, quality and single-crystal growth are more controllable compared with the other systems. Using first-principles band structure calculations, we focus on understanding the relationship between the crystal structure, charge doping and magnetism in $A$Fe$_2$As$_2$ systems. We will elaborate on the tetragonal to orthorhombic structural distortion along with the associated magnetic order and anisotropy, the influence of doping on the $A$ site and the Fe site and the changes in the electronic structure as a function of pressure. Experimentally, we investigate the substitution of Fe in SrFe$_{2-x}$TM$_x$As$_2$ by other 3d transition metals, $TM$ = Mn, Co or Ni. In contrast to a partial substitution of Fe by Co or Ni (electron doping), a corresponding Mn partial substitution does not lead to the suppression of the antiferromagnetic order or the appearance of superconductivity. Most of the calculated properties agree well with the measured properties, but several of them are sensitive to the As $z$ position. For a microscopic understanding of the electronic structure of this new family of superconductors, this structural feature related to the Fe–As interaction is crucial, but its correct *ab initio* treatment still remains an open question.

[1] Authors to whom any correspondence should be addressed.

**IOP** Institute of Physics 🝔 DEUTSCHE PHYSIKALISCHE GESELLSCHAFT

**Contents**

**1. Introduction**

The physics community around the world has been tirelessly working for the past few months to find different ways of increasing the superconducting transition temperature $T_c$ following the discovery of superconductivity at 26 K in the rare-earth-based ($RE$OFeAs) system $LaO_{1-x}F_xFeAs$ ($x = 0.05$–$0.12$) [1]. Spirited search by the experimentalists has led to eventually raising $T_c$ to 55 K for another member of this family of compounds, $SmFeAsO_{0.9}F_{0.1}$ [2]. Shortly afterwards, another family of Fe-based compounds, $AFe_2As_2$, ($A = $ Ca, Sr, Ba or Eu) was also found to be superconducting upon hole doping[2] on the $A$ site with a maximum of $T_c = 38$ K [3]–[5]. These discoveries were followed by the announcement of other new parent compounds: LiFeAs, FeSe and SrFeAsF with a maximum $T_c$ of 18 K [6], 14 K [6] (27 K using pressure [7]) and 56 K [8], respectively. The basic features that are common to many of these new parent compounds are the antiferromagnetic (AFM) ordering of the Fe spins at $T_N \approx 100$–$200$ K, and the quasi-2D nature of the electronic structure. All the members belonging to the above-mentioned families have been shown to superconduct upon either 'hole' or 'electron doping' only with the exception of LiFeAs, wherein it is considered that the Li layer acts as a charge reservoir for the system [6]. Superconductivity also emerges upon application of hydrostatic pressure for certain members of the $RE$OFeAs, $AFe_2As_2$ and FeSe families. Notwithstanding the abundant research that has already been performed, the microscopic nature of the mechanism of superconductivity has remained elusive so far. A systematic study of the many members within one particular family, using both experimental and theoretical techniques, would pave the way to a more concrete understanding of the electronic structure of the normal state. Although the $RE$OFeAs systems have larger $T_c$ values, their sample preparation, characterization and quality, as is the case for many oxides, have to be considered with great care. Alternatively, it has been demonstrated that the $AFe_2As_2$

---

[2] Our nomenclature of '$-x$' means hypovalent subsitition, whereas '$x$' means hypervalent substitution.

systems could be synthesized comparatively more easily. Hence, here we carry out a systematic investigation using both theoretical and experimental techniques for the $A\mathrm{Fe_2As_2}$ systems.

All the $A\mathrm{Fe_2As_2}$ compounds crystallize in the tetragonal $\mathrm{ThCr_2Si_2}$-type structure at room temperature. They all exhibit a structural transition upon cooling to an orthorhombic lattice ($T_0$ is ∼171 K for Ca [9], ∼205 K for Sr [10], ∼140 K for Ba [11] and ∼200 K for Eu [12]). The structural transition is coupled with an AFM ordering of the Fe moments with a wave vector $Q = [1, 0, 1]$ for the spin-density-wave (SDW) pattern. Suitable substitution on either the $A$ site or the Fe site can suppress the magnetic ordering, and then the system becomes superconducting for certain ranges of doping (for example, maximum $T_c = 38$ K for $(\mathrm{Ba,K})\mathrm{Fe_2As_2}$ [5], 32 K for $(\mathrm{Eu,K})\mathrm{Fe_2As_2}$ [13], 21 K for $\mathrm{Sr(Fe,Co)_2As_2}$ [14] and $\mathrm{Ba(Fe,Co)_2As_2}$ [15]). Superconductivity can also be induced in 'undoped' and 'under-doped' compounds by applying pressure [16].

In the following sections, we describe the microscopic picture of the magneto-structural transition and the effects of external pressure, chemical pressure and charge doping on the $A\mathrm{Fe_2As_2}$ systems. In order to make the paper more easily readable, we introduce the following abbreviations: $RE\mathrm{OFeAs}$: 1111; $A\mathrm{Fe_2As_2}$: 122; $\mathrm{LiFeAs}$: 111; $\mathrm{FeSe}$: 11; $\mathrm{SrFeAsF}$: 1111′; non-magnetic: NM; ferromagnetic: FM; checkerboard nearest neighbour AFM: NN-AFM; columnar/stripe-type AFM order of the Fe-spins: SDW (spin-density-wave).

## 2. Methods

### 2.1. Theory

We have performed density functional band structure calculations using a full potential all-electron local orbital code, FPLO [17, 18][3], within the local (spin) density approximation (L(S)DA) including spin–orbit coupling when needed. The Perdew–Wang [19] parametrization of the exchange-correlation potential is employed. Density of states (DOS) and band structures were calculated after converging the total energy on a dense $k$-mesh with $24 \times 24 \times 24$ points. The strong Coulomb repulsion in the Eu 4f orbitals is treated on a mean field level using the LSDA + $U$ approximation in the atomic-limit double counting scheme [20]. The results we present below use the LSDA + $U$ method [21] in the rotationally invariant form [22]. In accordance with the widespread belief that in the new Fe-based superconducting compounds the Fe 3d electrons have a more itinerant character than a localized one, and thereby are much less correlated in comparison to the Cu 3d electrons in the high-$T_c$ cuprates, we did not apply the LSDA + $U$ approximation to the Fe 3d states. The effects of doping on either the cation site or the Fe site were studied using the virtual crystal approximation (VCA) treatment. The results obtained via VCA were cross checked using supercells for certain doping concentrations. The crystal structures are optimized at different levels to investigate or isolate effects that may depend sensitively on certain structural features. The full relaxation of the unit cell of the 122 systems at low temperatures involves optimizing $a/b$ and $c/a$ ratios in addition to relaxing the As $z$ position.

---

[3] We used version 7.00 of the FPLO release for all calculations pertaining to structural and magnetic transitions, doping and pressure effects. For the calculation of the electric field gradient (EFG), version 5.19 was used. As the basis set, Ca (3s3p/4s4p3d + 5s5p), Sr (3d4s4p/5s5p4d + 6s6p), Ba (4d5s5p/6s6p5d + 4f7s7p), Fe (3s3p/4s4p3d + 5s5p) and As (3s3p3d/4s4p4d + 5s5p) were chosen for semicore/valence + polarization states. The high-lying states improve the basis, which is especially important for the calculation of the EFG.
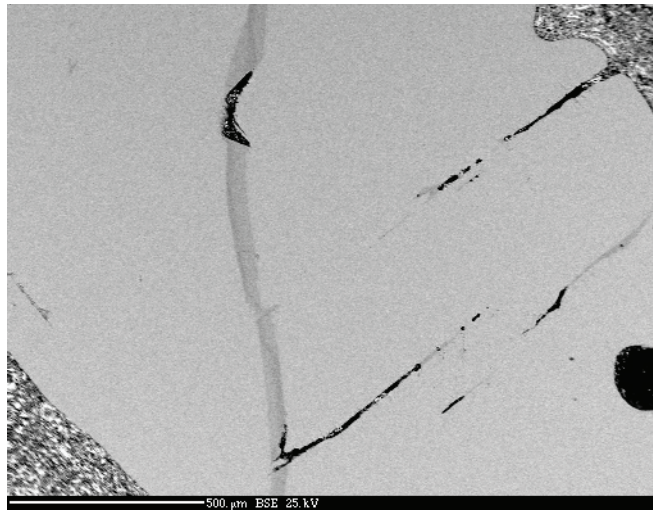
**Figure 1.** Micrograph of a polished crystal from the same batch from which crystal X2 was selected. Light grey phase: bulk crystal. Dark grey phase: inclusions of flux. Black regions: micro-cracks and cavities.

## 2.2. Experimental

Polycrystalline samples were prepared by sintering in glassy-carbon crucibles, which were welded into tantalum containers and sealed into evacuated quartz tubes for heat treatment at $900\,°C$ for $16\,h$ with two regrinding and compaction steps. First precursors SrAs, $Co_2As$, $Fe_2As$, $Mn_2As$ and NiAs were synthesized from elemental powders sintered at $600\,°C$ for $48\,h$ (Mn, Fe, Co and Ni 99.9 wt%; As 99.999 wt%; Sr 99.99 wt%). These educts were powdered, blended in stoichiometric ratios, compacted to pellets and heat treated. All sample handling was done inside argon-filled glove boxes. Crystals were grown in glassy-carbon crucibles by a modified self-flux method [15, 23] in melts with compositions $SrFe_{5-x}Co_xAs_5$ ($0.5 \leqslant x \leqslant 0.85$) by cooling from 1250 to $1100\,°C$ within $48\,h$. The melt was spun off at $1100\,°C$ using a centrifuge [25]. Metallographic investigations were performed on polished surfaces of selected secured crystal platelets. Electron-probe microanalysis (EPMA) with wavelength-dispersive analysis was accomplished in a Cameca SX100 machine. Crystal X1 was grown in a flux $SrFe_{4.25}Co_{0.75}As_5$ and crystal X2 in a flux $SrFe_{0.15}Co_{0.85}As_5$. For crystal X1 from EPMA the composition (in at.%) $Sr_{19.9(2)}Fe_{36.2(1)}Co_{4.2(1)}As_{39.7(1)}$ was found, which corresponds to $SrFe_{2-x}Co_xAs_2$ with $x \approx 0.21$. For crystal X2 from EPMA the composition (in at.%) $Sr_{19.5(2)}Fe_{35.5(1)}Co_{5.0(2)}As_{39.9(2)}$ was found, which corresponds to $SrFe_{2-x}Co_xAs_2$ with $x \approx 0.25$. Crystals grown from a flux $SrFe_{4.5}Co_{0.5}As_5$ had a composition of $Sr_{19.9(3)}Fe_{36.9(1)}Co_{3.2(1)}As_{39.9(2)}$ corresponding to $SrFe_{2-x}Co_xAs_2$ with $x \approx 0.15$ and showed no superconductivity. All crystals grown up to now exhibit some inclusions of flux material, which can be seen in figure 1 (for crystal X2 the second phase has the composition $Sr_{3(1)}Fe_{44(1)}Co_{8(1)}As_{45(1)}$ (in at.%)).

## 3. Results—theory

### 3.1. Ambient-temperature phase: tetragonal

We begin with comparing the DOS computed for a representative member of each family of the iron pnictide compounds. In these calculations, experimental values of the ambient-temperature

tetragonal lattice parameters and atomic positions were used for all the systems. Collected in figure 2 are the NM total and orbital-resolved DOS for five systems: 1111, 122, 111, 11 and 1111'. The states close to the Fermi energy ($E_F$) in all these systems consist mainly of Fe 3d contributions. The contribution of the pnictide atom (or Se in the case of FeSe) to the Fermi surface is small but nonzero. A pseudo-gap-like feature in the DOS slightly above the $E_F$ is common to all the systems. At the outset, all the five systems look quite similar to one another, but slight differences are already visible when analysing the Fe 3d orbital-resolved DOS, presented in the right panels of figure 2. The contribution of the Fe $3d_{x^2-y^2}$ orbital (the orbital pointing directly towards the NN Fe ions) is the largest close to $E_F$ for all the systems. The corresponding bands (not shown here) are highly dispersive in the $a$–$b$ plane and remain flat along the $c$-axis, indicative of the quasi-2D nature of this band. The distance of the $3d_{x^2-y^2}$ edge from the $E_F$ varies for the different systems and is the largest for the 111 family and smallest for the 1111 family. The second largest contribution to the Fermi surface comes from the doubly degenerate $3d_{xz}$ and $3d_{yz}$ orbitals and this feature is again consistent for all the iron pnictide compounds.

### 3.2. Structural distortion versus magnetic order

*3.2.1. Tetragonal to orthorhombic distortion.*　As discussed above, the FeAs-based compounds crystallizing in different structures have very similar electronic properties. However, between the 1111 and the 122 families there is an important difference in regard to structural and magnetic transitions. In the former, the transition temperatures for the structural transition are 10–20 K higher than those of the magnetic one. On the other hand, for the 122 family the structural and the magnetic transitions are found to be coupled and occur at the same temperature. By first-principles calculations, we explored the nature of this intimate connection between the two transitions for the 122 systems.

We calculated the total energies for different $b/a$ ratios for different magnetic models. For the NM, FM (not shown) as well as the NN-AFM (figure 3, upper panel) patterns, the lowest total energy occurred at $a = b$, indicating that for these patterns the tetragonal structure is more stable than the orthorhombic structure. Inclusion of spin–orbit effects did not change this result. The tetragonal to orthorhombic distortion is obtained only for the SDW pattern as displayed in the lower panel of figure 3. Hence, LSDA calculations clearly show that the SDW state is necessary for the tetragonal-to-orthorhombic transition to take place. The size of this effect, namely the deviation of the calculated $b/a$ ratio from unity, depends on the size of the cation, the ratio being smallest in $BaFe_2As_2$ and largest in $CaFe_2As_2$. The values obtained via LSDA are collected in table 1 and compared with the experimental reports. The trend obtained in LSDA fits well with the experimental $b/a$ ratios with the exception of $CaFe_2As_2$. Experimentally, $CaFe_2As_2$ crystals are shown to have complex microstucture properties. Recent studies using transmission electron microscopy (TEM) [28] have shown a pseudo-periodic modulation and structural twinning arising from tetragonal to orthorhombic transition only in $CaFe_2As_2$ but not in Sr or Ba 122 systems. A structural twinning hinders the correct estimation of the lattice parameters and may thereby explain the experimental deviation in the trend of the $b/a$ ratio for $CaFe_2As_2$ with respect to LSDA.

In all four compounds the coupling along the shorter in-plane axis is FM in agreement with experimental findings. Although these results are robust with respect to details of structure and calculations, the preferred direction of the spins is found to be quite sensitive. We performed
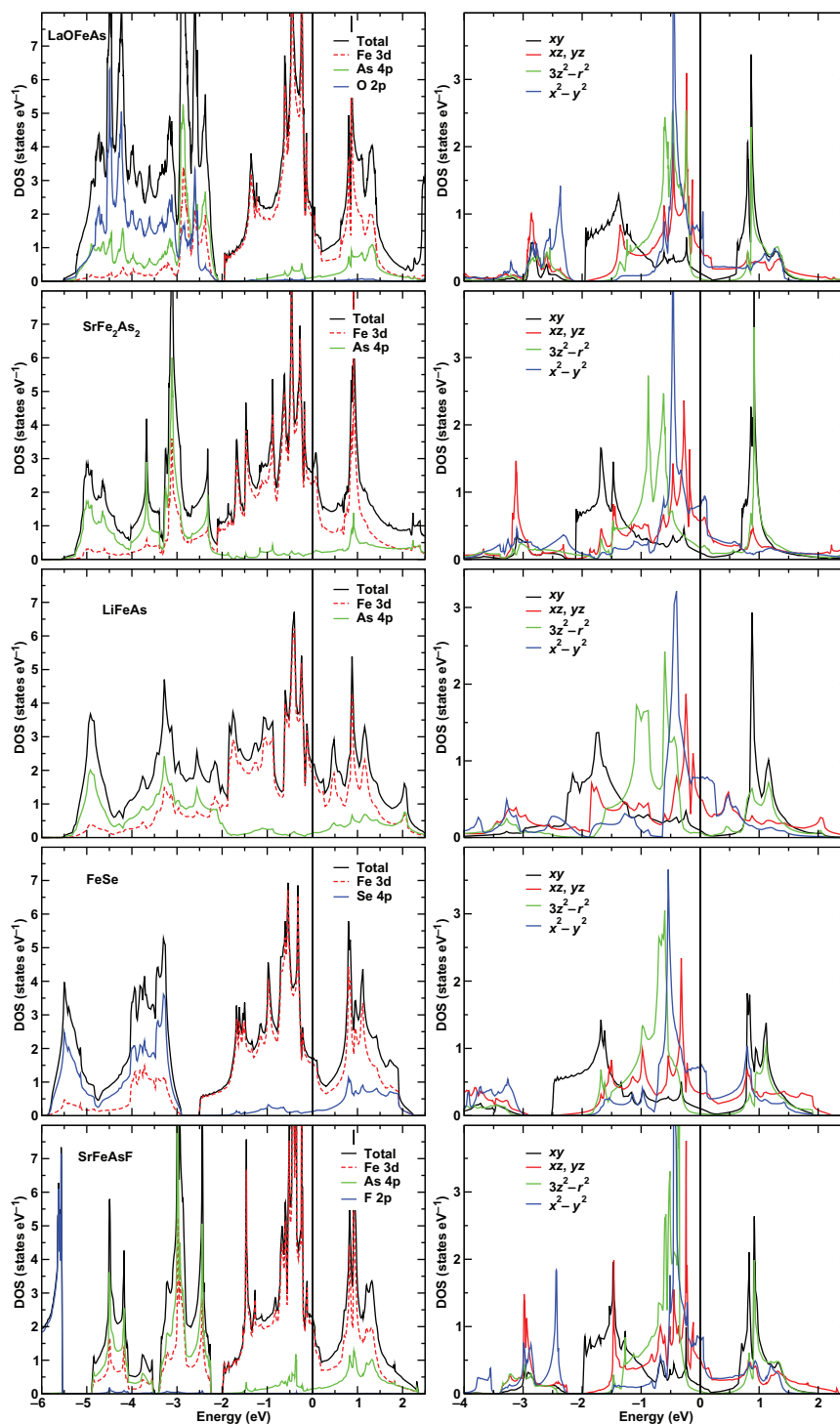
**Figure 2.** Comparison of total and site-resolved DOS per cell (left panel) and Fe 3d orbital-resolved DOS (right panel) of a representative member for each of the new superconducting family of compounds. LaOFeAs: 1111; $SrFe_2As_2$: 122; LiFeAs: 111; FeSe: 11; SrFeAsF: 1111′. The solid vertical lines at zero energy denote the Fermi level $E_F$.
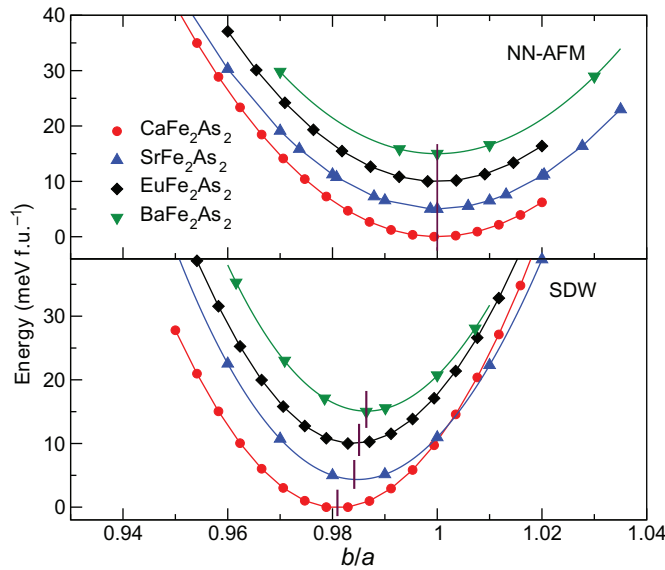
**Figure 3.** Total energy as a function of $b/a$ for the $A\mathrm{Fe_2As_2}$ ($A = \mathrm{Ca}$, Sr, Eu, Ba) systems with two possible spin arrangements between the Fe spins. In NN-AFM the spins of all the NNs are anti-parallel to each other. In the SDW pattern, the spins along the longer $a$-axis are anti-parallel, whereas the spins along the shorter $b$-axis are parallel. The solid vertical lines denote the minimum value of the energy. The minimum energy for each system has been set to zero. For clarity, Sr122, Eu122 and Ba122 curves are offset by 5, 10 and 15 meV.

fully relativistic calculations for the $A = \mathrm{Ca}$, Sr and Ba cases using (i) SDW with $Q = [1\ 0\ 0]$ and (ii) SDW with $Q = [1\ 0\ 1]$. The latter SDW pattern requires the doubling of the $c$ lattice parameter and the corresponding calculations are highly time consuming. Therefore, only the Cartesian axes are considered for possible spin orientations, and the structural data corresponding to the minima in figure 3 are used. In the Sr122 case for both SDW patterns, we find the direction of the AFM coupling (along the longer $a$-axis) as the easy axis in agreement with the neutron scattering study result [26]. However, in the Ca and Ba 122 cases, different axes in the $(a, b)$ plane are found as easy axes for different SDW patterns. The longer axis, the $a$-axis, is the easy axis for Ba (Ca) 122 for $Q = [1\ 0\ 0]$ ($Q = [1\ 0\ 1]$); the shorter axis, $b$, is the direction of FM coupling for Ba (Ca) 122 for $Q = [1\ 0\ 1]$ ($Q = [1\ 0\ 0]$). Since the involved energy differences are tiny (of the order of 15–30 $\mu$eV per atom), a satisfactory resolution of this issue requires further study. On the other hand, the experimental study of Ba122 [29] has been able to determine only spins that lie in the $(a, b)$ plane.

*3.2.2. Plasma frequency and effective dimensionality.*    Band structure calculations can provide information on the 'effective dimensionality' in a compound through various means, such as dispersionless (flat) energy bands along certain symmetry lines, van Hove singularities in DOS, etc. A simple quantitative measure, however, can be obtained by computing plasma frequencies along the main unit cell axes. For all of the 122 compounds as well as the representative compounds for the other families, plasma frequencies are calculated by NM calculations using the experimental structural data of the tetragonal phase. In table 2, we present the ratio of the in-plane plasma frequency ($\omega_P^a = \omega_P^b$) to the plasma frequency along the $c$-axis ($\omega_P^c$). One notices

**Table 1.** Comparison of $b/a$ obtained from LSDA for the SDW pattern with experimental reports. The references from which the experimental numbers are obtained are indicated. With the exception of Ca122 (for a more detailed discussion, see the text), the trend in the in-plane axis distortion for the orthorhombic structure is consistent with experimental findings.

|       | $b/a$—LSDA | $b/a$—expt | Reference |
| ----- | ---------- | ---------- | --------- |
| Ca122 | 0.9809     | 0.9898     | [25]      |
| Sr122 | 0.9841     | 0.9889     | [26]      |
| Eu122 | 0.9850     | 0.9898     | [27]      |
| Ba122 | 0.9864     | 0.9928     | [11]      |

**Table 2.** Ratio of the in-plane plasma frequency $\omega_P^a$ to the out-of-plane plasma frequency $\omega_P^c$ for various members of the Fe-based superconducting systems. The observed trend in the plasma frequency ratios follows the trend in the ratios of the (interlayer to intralayer) Fe–Fe distances, $d_c^{Fe-Fe}/d_a^{Fe-Fe}$. As we go down the column, the systems go from being more 2D towards being more 3D. The maximum superconducting transition temperature $T_c^{max}$ obtained either via doping or pressure is also collected in the last column. The trend in $T_c^{max}$ also follows the trend in $\omega_P^a/\omega_P^c$, with decreasing temperatures when the systems become more 3D.

|          | $\omega_P^a/\omega_P^c$ | $c/a$ | $d_c^{Fe-Fe}/d_a^{Fe-Fe}$ | $T_c^{max}$ (K) |
| -------- | ----------------------- | ------ | ------------------------- | --------------- |
| SrFeAsF  | 19.892                  | 2.2426 | 3.1715                    | 56 [8]          |
| LaOFeAs  | 8.9467                  | 2.1656 | 3.0626                    | 55 [2]          |
| FeSe     | 4.1119                  | 1.4656 | 2.0727                    | 27 [7]          |
| LiFeAs   | 3.2181                  | 1.6785 | 2.3738                    | 18 [6]          |
| $BaFe_2As_2$ | 3.2926              | 3.2850 | 2.3228                    | 38 [5]          |
| $SrFe_2As_2$ | 2.8329              | 3.1507 | 2.2279                    | 38 [4, 5]       |
| $CaFe_2As_2$ | 1.3953              | 3.0287 | 2.1416                    | 20 [30]         |

that for the 122 family the results are in line with expectations: the compound is least anisotropic (more 3D-like) for the smallest cation (Ca) and strongly anisotropic (less 3D-like) for the largest cation (Ba). Additionally, the 1111 and 1111′ families are seen to be much more anisotropic (more 2D-like) than all of the others.

In the case of iron arsenides, in a rather simplified picture, one expects the plasma frequency ratio to be proportional to the ratio of the shortest interlayer ($d_c^{Fe-Fe}$) to the shortest intralayer Fe–Fe distances ($d_a^{Fe-Fe}$). In terms of lattice parameters the distance ratio $d_c^{Fe-Fe}/d_a^{Fe-Fe}$ is $c/\sqrt{2a}$ for 122's and $\sqrt{2c}/a$ for the others. Table 2 shows that these two ratios are largely correlated with each other with, apparently, the exception of FeSe[4].

---

[4] Note that the structural parameters for FeSe are taken from a very old reference, and that plasma frequencies depend sensitively on the band structure, which in turn can be affected strongly by the details of the crystal structure.

**Table 3.** Comparison of the magnetic moments in $\mu_B$ per atom calculated using LSDA with the experimental values obtained via $\mu$SR (a local probe) and neutron diffraction measurements. In LSDA, the moments were calculated for the SDW pattern for the Fe spins using a tetragonal lattice ($a = b$) and an orthorhombic lattice ($a \neq b$). The Fe–As distance has been optimized for all the calculations reported in this table.

| | LDA—SDW | | | Neutron |
| | $a = b$ | $a \neq b$ | $\mu$SR | diffraction |
| --- | --- | --- | --- | --- |
| Ca122 | 0.818 | 0.875 | 0.9 [33] | 0.80 [34] |
| Sr122 | 1.1 | 1.13 | 0.8 [33] | 0.94 [35] |
| Ba122 | 1.12 | 1.17 | 0.5 [33] | 0.87 [36] |

*3.2.3. Effect of the As z position and magnetic moments from LDA.*  In any first-principles study of a magnetic system, an essential aspect is the comparison of the computed magnetic moments with the experimentally deduced ones. This standard procedure proves to be quite tricky in these FeAs-based compounds due to the unexpected sensitivity of the magnetism to the As *z* position [31]. We performed a series of calculations[5] for Ca, Sr and Ba 122 systems for FM, NN-AFM and SDW spin patterns using the experimental volume (ambient pressure, below $T_N$) both with $a = b$ and $a \neq b$ and optimizing the Fe–As distance (via the As *z* position) for each case. Table 3 compares the Fe moments computed for the SDW pattern (the lowest-total-energy spin pattern among those considered) with the experimental values obtained using neutron diffraction and muon spin rotation ($\mu$SR). In comparison to the situation in the 1111 systems, here for the 122 systems, the agreement between theory and experiment is seen to be better. However, the computed Fe magnetic moment is found to increase from Ca to Ba 122, whereas the trend is just the opposite according to the estimation of moments from $\mu$SR results. The moments obtained from neutron diffraction experiments are more reliable and remain rather constant for the three 122 systems considered here. The influence of the orthorhombic distortion on the calculated moments is quite negligible.

The better agreement between theory and experiment regarding the Fe magnetic moment in the case of 122 systems can be understood as follows. The computed versus measured magnetic moment discrepancy in the 1111 systems is usually explained to be a result of large spin fluctuations [32]. It is also known that spin fluctuation effects are reduced when going from 2D systems to 3D systems. Hence, the results presented in table 3 provide additional support for the effective dimensionality considerations described above: the 122 systems have a more pronounced 3D nature than the 1111 systems. Since the description of spin fluctuation effects is insufficient in LSDA, the computed values are immune to such effects, while, of course, the values deduced from experiments do reflect these effects. Furthermore, since the Ba 122 system is more 2D-like than the Ca 122 system (cf table 2), it is expected to exhibit a smaller Fe moment (stronger spin fluctuation effects), and this is in agreement with the $\mu$SR results.

The interplay between the Fe–As distance and different magnetic long-range orders is illustrated in figure 4 for $SrFe_2As_2$. Similar results are found for the other 122 systems.

---

[5] Experimentally, the Eu spins in $EuFe_2As_2$ are shown to order antiferromagnetically in the *a–b* plane. This in turn doubles the unit cell along the *c*-axis during the LDA + *U* calculations and introduces two inequivalent As positions. Optimizing the Fe–As distance for this scenario is more time consuming and is therefore postponed.
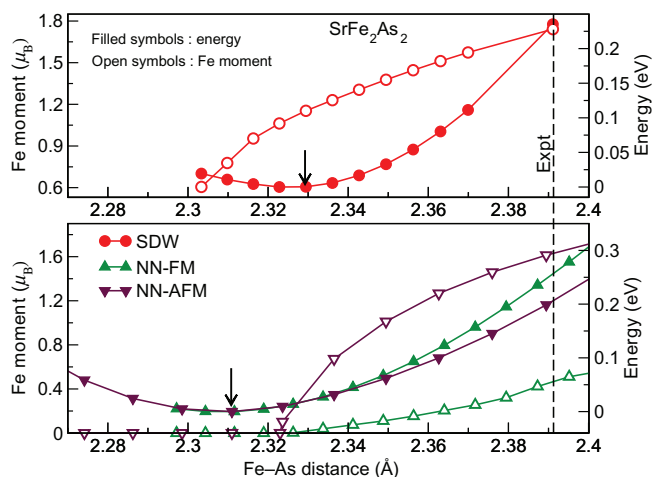
**Figure 4.** Energy and Fe magnetic moment as a function of the Fe–As distance using different spin patterns for $SrFe_2As_2$ at the experimental volume around 90 K [27]. Optimization using FM and NN-AFM pattern leads to an NM solution, while the SDW pattern stabilizes with an Fe moment of $1.13\mu_B$. The energy curves have been shifted by setting the minimum energy value to zero. The dashed vertical line refers to the experimental Fe–As distance obtained from [27]. The arrows indicate the position of the energy minima.

The experimental value of the Fe–As distance in $SrFe_2As_2$ in the orthorhombic phase is reported to be 2.391 Å at 90 K [27]. Using the FM or the NN-AFM spin pattern produces a minimum in energy at about 2.31 Å along with a complete loss of the Fe magnetic moment. In the SDW pattern, the optimum value of the Fe–As distance is 2.327 Å, only slightly larger than that obtained using the FM or NN-AFM pattern, but the Fe magnetic moment is still $1.13\mu_B$.

The As $z$ position is most likely one of the key issues for understanding the iron pnictides. Present day density functional theory (DFT)-based calculations using LDA (described above) and also generalized gradient approximation (GGA) [31, 37] are not able to reproduce all the experimental findings consistently. Since the magnetism and therefore the superconductivity crucially depend on this structural feature and the related accurate description of the Fe–As interaction, the improvement of the calculations in this respect may offer the key to the understanding of superconductivity in the whole family.

### 3.3. Effects of pressure

As mentioned above, superconductivity in the FeAs-based systems can be achieved via doping of charge carriers. This kind of chemical substitution is quite convenient, but changes the electronic structure of the doped systems in a nontrivial way as compared with the undoped systems. Using external pressure as a probe on these systems creates a similar effect as doping, without the added complexity. Application of hydrostatic pressure suppresses both the tetragonal to orthorhombic distortion and the formation of the SDW, and leads to the onset of superconductivity in a similar fashion as charge doping. All the parent members of the 122 family have been reported to superconduct or show signs of its onset under pressure [16, 25], [38]–[40]. Ca122 was originally reported to superconduct ($T_c \approx 10$ K) at
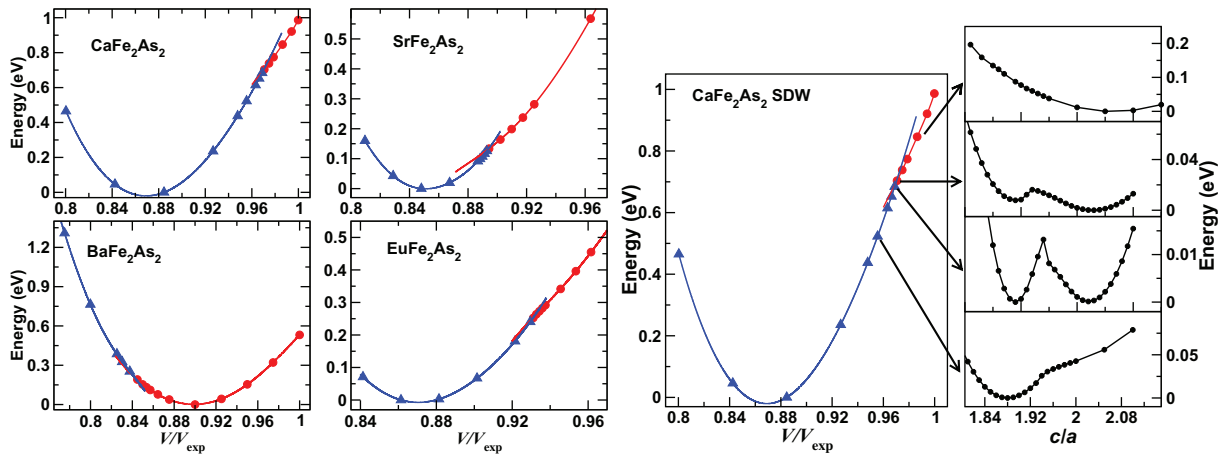
**Figure 5.** Left panel: energy as a function of volume for the $A$Fe$_2$As$_2$ systems, with the $c/a$ ratio optimized. The two curves correspond to the antiferromagnetically ordered Fe spins in the SDW pattern with a nonzero moment (red circles) and zero moment (blue triangles). The kink at the intersection of these two curves is caused by a collapse of the $c/a$ ratio upon pressure, which happens at the juncture when the systems lose their Fe moments and become NM. The $c/a$ ratio collapse is most pronounced in CaFe$_2$As$_2$ due to the small size of the Ca ion, and as the size of the $A$ ions increases, this feature becomes more and more subtle. Right panel: the evolution of the $c/a$ ratio collapse for CaFe$_2$As$_2$. Notice the emergence of the double minima.

0.4 GPa pressure [25, 38] but recently Yu and collaborators [41] did not observe any signature of bulk superconductivity and suggested a possible phase separation due to non-hydrostatic conditions. Similarly, Sr122 was first reported to superconduct at 2.8 GPa pressure with a $T_c$ of 27 K [40], whereas, on the contrary, Kumar *et al* [16] did not observe a zero-resistance state up to 3 GPa pressure. A sharp drop in resistivity above 2 GPa pressure was reported for Eu122, suggesting the onset of superconductivity and, more interestingly, signatures of possible re-entrant superconductivity. Though there exist conflicting reports of the transition pressure and possible phase separation in the sample under pressure, it is worthwhile to explore the evolution of the electronic structure and magnetism as a function of pressure. Pressure studies [25] on the CaFe$_2$As$_2$ system report a significant $c/a$ collapse along with a structural transition (orthorhombic to tetragonal) under modest pressures of less than 0.4 GPa, while no such collapse has been reported for the other compounds. X-ray diffraction refinements carried out at 180 K for SrFe$_2$As$_2$ [16] observe an orthorhombic to tetragonal transition above 3.8 GPa, but no collapse of the $c/a$ ratio is observed. Band structure calculations allow for the study of such features up to very large pressures, which might not be easily attainable through experiments. We have calculated energy as a function of volume for all the four systems in the 122 family. Firstly, we wanted to investigate the possibility of a $c/a$ collapse for each member of the 122 family. Therefore, we calculated energy as a function of volume using the SDW pattern and optimizing only the $c/a$ ratio at each volume. The internal As $z$ parameter was kept fixed at the experimental (room temperature) value. The results from these calculations are collected in figure 5. Surprisingly, all the four 122 systems have a kink in
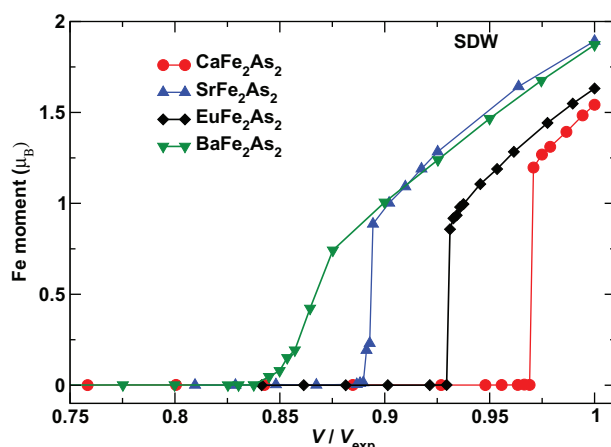
**Figure 6.** Volume dependence of the Fe moments corresponding to the energy–volume curves in figure 5. The quenching of the spin magnetic moment is highly abrupt for the compounds with pronounced $c/a$ ratio collapse. The Fe moment in $BaFe_2As_2$ goes to zero smoothly reflecting the much smoother $c/a$ variation obtained for this compound.

the energy–volume curve caused by a non-continous change in the $c/a$ ratio, which happens at the juncture when the systems lose their Fe moments and become NM (see figure 6). The sharpness of the kink is largest for Ca122 and decreases with increasing of the size of the $A$ ion. Such an $A$-ion size effect was also observed and discussed in section 3.2.1 when investigating the size of the orthorhombic $b/a$ ratio. Our result obtained from LSDA (via a common tangent construction) for $CaFe_2As_2$ is in excellent agreement with the previously reported [25] experimental data, volume collapse: $\delta V^{LDA} \approx 4.7\%$, $\delta V^{exp} \approx 5\%$; and ratio collapse: $\delta(c/a)^{LDA} \approx 9.8\%$, $\delta(c/a)^{exp} \approx 9.5\%$. Experimentally [27], a pressure of $\sim 0.3\,GPa$ induces a transition from the orthorhombic phase to a collapsed NM tetragonal phase for $CaFe_2As_2$. Scaling the volumes of the different 122 systems with respect to the experimental values ($V/V_{exp}$), one observes that the kink in the energy–volume curve for the other three 122 systems happens at lower volume ratios (or larger pressures) as compared with the Ca122. It should be worthwhile to investigate this structural feature experimentally by applying higher pressures to the Sr, Ba and Eu 122 systems.

Changes in the electronic structure as a function of reduced volumes were carefully monitored. Shown in figure 7 are the total DOS for $SrFe_2As_2$ at selected volumes. Similar results are obtained for other 122 systems. The DOS at $E_F$ decreases gradually at first for up to 10% volume reduction with respect to the experimental volume. The Fe ions continue to carry a magnetic moment though the actual values are quite reduced. Upon further reduction of the volume, the spin moments get quenched and the DOS at $E_F$ begins to increase and the system becomes NM. At the experimental volume, the net moments on the various Fe orbitals are quite similar; with the Fe $3d_{x^2-y^2}$ having a slightly larger value than the other orbitals. With the application of pressure, the net moments of all the five d orbitals decrease in a similar fashion and tend to zero.

Another important feature that needs to be addressed in regard to the energy–volume curves is the serious underestimation of the equilibrium volume within LDA. Generally, equilibrium volumes obtained from LDA are smaller within up to 8% of the experimentally reported values.
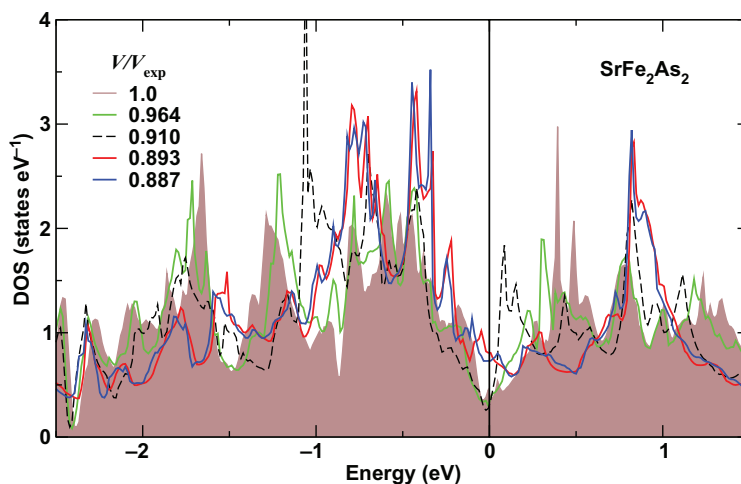
**Figure 7.** Total DOS per cell as a function of reduced volume for $SrFe_2As_2$ corresponding to the energy–volume curves in figure 5. In the SDW pattern, the total DOS for both the spin-up and spin-down channels are the same. Therefore, we show here the DOS from only one of the spin channels. The DOS at the Fermi level $E_F$ at first decreases with decreasing volume, but later starts to increase after the Fe spin magnetic moment is quenched.

In the case of 122 systems using the SDW pattern, we obtain values that are 13, 15, 10 and 13% smaller than the experimental reports for Ca, Sr, Ba and Eu 122 systems, respectively. Moreover, at the LSDA equilibrium volume, contrary to the experimental reports, all the parent compounds are computed to be NM. The reason for this discrepancy is unclear. In the previous sections we discussed the pronounced sensitivity of the Fe moments to the various structural parameters in these FeAs systems. Although with partial optimization (fixed As $z$ parameter) we have satisfactorily accounted for the experimentally observed $c/a$ collapse in $CaFe_2As_2$, it is necessary to find out what the ultimate LSDA solution is regarding the geometrical structure and magnetism in the 122 systems. Consequently, for Ca and Sr 122 systems and using the SDW pattern, at each volume we have optimized all three free structural parameters in the following order: (i) As $z$ position, (ii) $c/a$ ratio and (iii) $b/a$ ratio. This sequence of steps has been repeated until the energies obtained are converged to an accuracy of $10^{-6}$ eV. Collected in figure 8 are the energy–volume curves for the Ca and Sr 122 systems. The equilibrium volume obtained after a full optimization is only slightly larger than the values obtained after just a $c/a$ optimization (see figure 5). Contrary to the results depicted in figure 5, we now no longer observe any kink at the juncture when the Fe ions lose their magnetic moments. The loss of moment for Sr122 is more gradual than for Ca122. As volume is decreased (higher pressures are applied) the Fe spin magnetic moments tend to zero while the orthorhombic distortion ratio $b/a$ tends to unity so that at increased pressures the tetragonal lattice is favored. This observation of the lattice structure preferring the tetragonal symmetry when the Fe ions become NM is consistent with our previous results in section 3.2.1, and reaffirms the intimate connection between structure and magnetism for the 122 systems. Optimizing the As $z$ parameter again tends to confirm certain experimental findings (the connection between SDW magnetic pattern and orthorhombic distortion) but not all (for example, lack of $c/a$ collapse under pressure for $CaFe_2As_2$). This again re-affirms the need for a correct description of the Fe–As interplay to obtain consistent results.
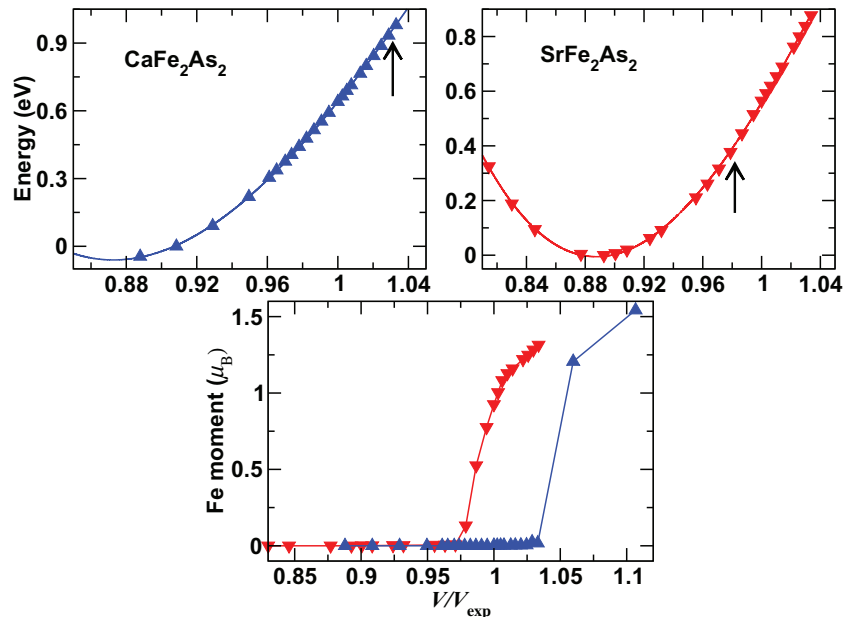
**Figure 8.** Top panel: energy as a function of volume after a full relaxation of all the parameters for $SrFe_2As_2$ and $CaFe_2As_2$. Contrary to the results depicted in figure 5, we now no longer observe any kink at the juncture when the Fe ions lose the magnetic moment (the corresponding data point is indicated using an arrow). Bottom panel: Fe magnetic moment as a function of volume for the Ca and Sr 122 systems. The results shown here are different from the moment values collected in table 3, because no $c/a$ optimization was carried out for the latter.

### 3.4. Effects of charge doping

In order to understand the influence of charge doping (both electrons and holes) on the electronic structure and henceforth the magnetism, we performed total energy calculations using the VCA for three different spin patterns: FM, NN-AFM and SDW. We considered both electron and hole doping on the $A$ site as well as the Fe site. Our results for the changes in the Fe moment in $SrFe_2As_2$ are collected in figure 9. Similar results were obtained for other members of the 122 family. We observe very different effects depending on the sign (electrons or holes) and site (Sr or Fe) of the doping. Regardless of the choice of magnetic ordering, electron doping on the Fe (Sr) site weakens (enhances) the magnetism. This behaviour can be explained by analysing how the NM electronic structure changes with electron doping (see figure 10). Electron doping on the Fe site (top left panel of figure 10) results in DOS very similar to that of the undoped case, the main effect being that the $E_F$ moved towards higher energies to accommodate the added electrons. On the other hand, electron doping on the Sr site changes the resultant DOS drastically (see the top left and the right panel of figure 10). Most of the major changes to DOS occur in the close vicinity of $E_F$, giving rise to pronounced peaks at the $E_F$. A large value of DOS at the Fermi level, $N(E_F)$, is usually a sign of instability for an electronic system. The system can lower $N(E_F)$ by, for example, developing a long-range magnetic order provided the Stoner criterion is satisfied. The larger values of the computed Fe magnetic moments may reflect such an increased instability to magnetic order. Additionally, with reservations for possible
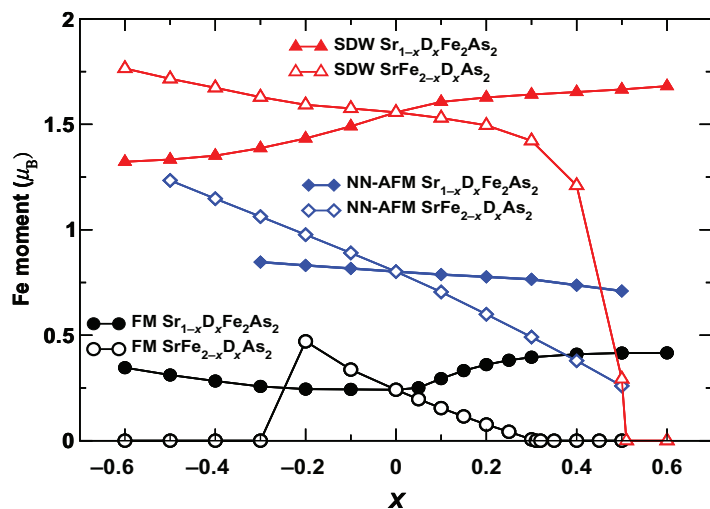
**Figure 9.** Results from the VCA calculations. Magnitude of the Fe moment as a function of charge doping (both on the Sr site as well as on the Fe site) for different ordering patterns in $SrFe_2As_2$. When $x$ is positive: electron doping; when $x$ is negative: hole doping. The filled symbols and the open symbols indicate doping of the $A$ site and the Fe site, respectively. 'D' represents the dopant. Very different effects are observed when doping charge carriers on the Sr or Fe site. Magnetism is weakened when electrons are substituted on the Fe site and strengthened when electrons are substituted on the Sr site. The relative trend between the different ordering patterns remains the same. We have used the experimental lattice parameters (at $\approx 300\,K$) and the As $z$ value for all the calculations.

thermodynamic considerations, appearance of this feature may explain why La doped 122 samples could not be synthesized until now.

Substitution of holes on the Sr site does not introduce significant changes to the Fe magnetic moment. Substitution of holes on the Fe site tends to enhance magnetism for both AFM patterns, whereas for the FM pattern the magnetism vanishes beyond a critical level of doping. However, this feature for the FM spin pattern is of no significance, because energetically it lies above both of the AFM patterns at all levels of doping.

## 3.5. Electric field gradient (EFG)

Nuclear magnetic resonance (NMR) is a local probe that is extremely sensitive to certain details of the structure. Since the As $z$ position is a key determinant of many of the electronic properties of the FeAs systems, the quadrupole frequency $\nu_Q$ from NMR measurements can provide a direct measure of the Fe–As interaction. Theoretically, $\nu_Q$ can be obtained by calculating the EFG. The EFG is defined as the second partial derivative of the electrostatic potential $v(\vec{r})$ at the position of the nucleus

$$V_{ij} = \left( \partial_i \partial_j v(0) - \tfrac{1}{3} \Delta \delta_{ij} v(0) \right). \tag{1}$$
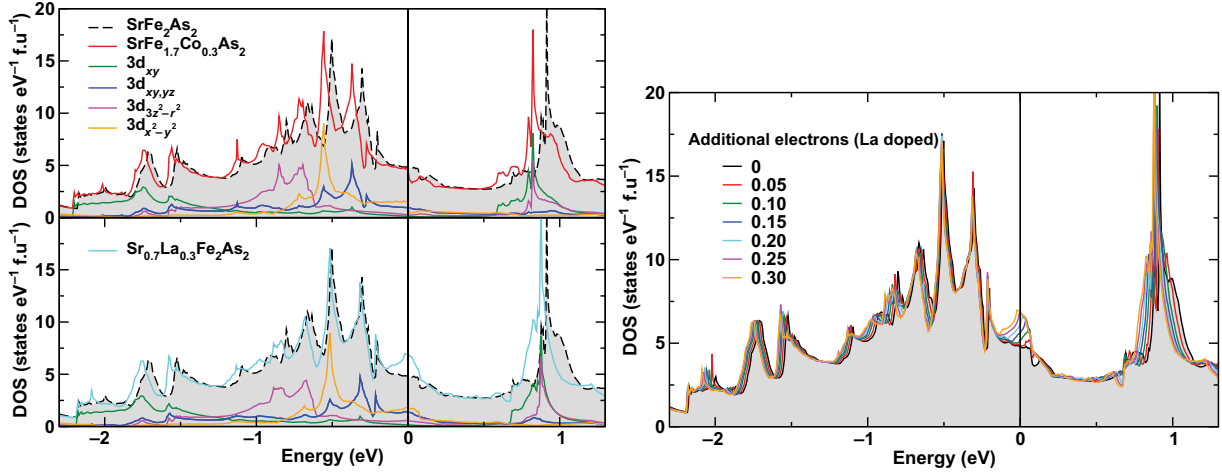
**Figure 10.** Top left panel : NM total and Fe orbital-resolved DOS from a VCA calculation for a 15% electron doping on the Fe site in Sr122. Upon electron doping, the DOS remains unchanged and displays a rigid-band-like behaviour. Bottom left panel: NM total and Fe orbital-resolved DOS for a 30% electron doping on the Sr site in Sr122. Addition of electrons changes the shape of the DOS close to $E_F$ drastically. A pronounced peak starts to appear close to $E_F$, which tends to destabilize the system. The changes in the total DOS for various doping concentrations are shown in the right panel. Right panel: NM total DOS as a function of additional electrons on the Sr site in Sr122.

This traceless and symmetric tensor of rank 2 is described in the principal axis system by the main component $V_{zz}$ and the asymmetry parameter $\eta = (V_{xx} - V_{yy})/V_{zz}$. $V_{zz}$ is as per definition the component with the largest magnitude $|V_{zz}| \geqslant |V_{yy}| \geqslant |V_{xx}|$ and is not necessarily parallel to the $z$-axis of the crystal. From these two parameters ($V_{zz}$ and $\eta$) and the quadrupole moment for $^{75}$As $Q = (0.314 \pm 0.006)$ barn [42], the quadrupole frequency $\nu_Q$ for $^{75}$As (with a nuclear spin of $I = 3/2$) can be calculated [43] as

$$\nu_Q = \frac{eQV_{zz}}{2h}\sqrt{1 + \frac{\eta^2}{3}}. \tag{2}$$

The experimental lattice parameters including the As $z$ position for the calculation of the EFG for As in CaFe$_2$As$_2$, SrFe$_2$As$_2$ and BaFe$_2$As$_2$ were obtained from [11, 25][6]. For the parent compounds, we investigated the influence of the As $z$ position, the structural phase transition, the magnetism and the pressure on the EFG. We also investigated the effects of doping on the EFG.

First we focus on the As $z$ dependence of the EFG. As in the case of the computed Fe magnetic moment, whose value shows a strong dependence on the As $z$ position (see section 3.2.3), the EFG is also found to display a strong As $z$ dependence. The EFG increases strongly for all three compounds, as the Fe–As distance decreases, see figure 11. In the case of CaFe$_2$As$_2$, there is a minimum in the EFG for a displacement of roughly $\Delta z = -0.1$ Å from the experimental position, whereas for larger Fe–As distances the EFG increases again. The same

---

[6] Tetragonal phase: $a = 3.9250$, $c = 12.332$, $z(As) = 0.358$; orthorhombic phase: $a = 5.5819$, $b = 5.5197$, $c = 12.332$, $z(As) = 0.358$ for SrFe$_2$As$_2$.
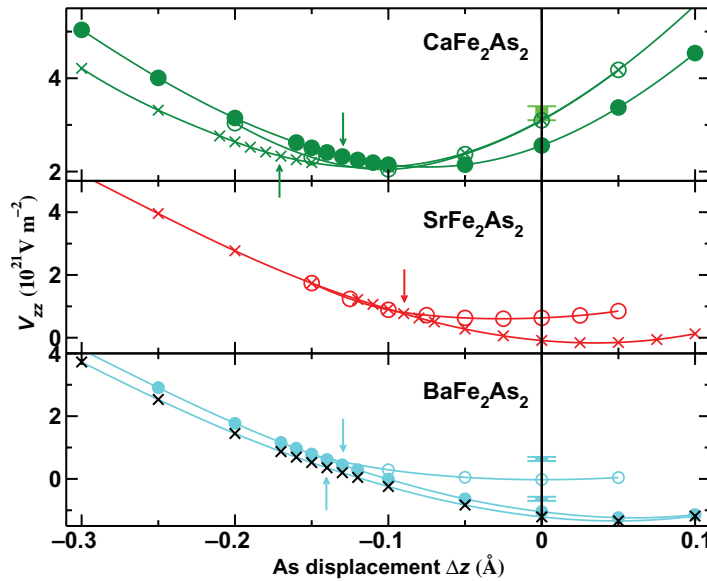
**Figure 11.** Dependence of the EFG for As on the As $z$ position. $\Delta z = z - z_{exp}$. Different symbols show different calculations: cross: NM with tetragonal symmetry; full circle: NM with orthorhombic symmetry (almost identical to tetragonal symmetry for $SrFe_2As_2$ and therefore not shown): and empty circle: magnetic (SDW pattern) with orthorhombic symmetry. The total energy minimum is marked by an arrow for each NM curve. The error bars show the experimental results for the tetragonal phase (at 250 K for $CaFe_2As_2$ and at 200 K for $BaFe_2As_2$ (the two error bars indicate the experimentally unknown sign of the EFG).

trend is observed for the other two compounds (middle and lower panels of figure 11). They exhibit the minimum in the EFG at about $\Delta z = +0.05$ Å. For all the three parent compounds, the Fe–As distance at which the minimum of total energy occurs is smaller than that corresponding to the EFG minimum (see arrows in figure 11). For $CaFe_2As_2$ we observe good agreement between the calculated EFG at the experimental As $z$ position (for 250 K) and the measured EFG at 250 K [44] (the light green symbol in the upper panel of figure 11). In the case of $BaFe_2As_2$ the magnitude of the measured EFG at 200 K is roughly $0.7 \times 10^{21}$ V m$^{-2}$ [45], while the sign is unknown since it cannot be extracted from nuclear quadrupole resonance (NQR) measurements (in figure 11 the experimental EFG values with both signs are shown). The calculated $V_{zz}$ for the experimental As $z$ position is $-1.1 \times 10^{21}$ V m$^{-2}$. If the experimental EFG is negative, reasonable agreement between experiment and calculation is obtained. In a preliminary measurement for $SrFe_2As_2$ the quadrupole frequency $\nu_Q$ was determined to be less than 2 MHz [46], and this is also consistent with the calculated quadrupole frequency of 0.8 MHz at the experimental As $z$ position. For members of the 1111 family, namely LaFeAsO and NdFeAsO, the calculated EFG for the optimized As $z$ position agreed well with the experimental EFG [47, 48]. Our results for three representative members of the 122 family as shown above follow a different trend: the calculated EFG using the experimental As $z$ position agrees well with the measured EFG values.

To study the influence of the orthorhombic distortion, but without the influence of magnetism, we perform NM calculations both in tetragonal and orthorhombic symmetry.

**Table 4.** $V_{zz}$ in $10^{21}\,V\,m^{-2}$ for the NM and different magnetic orders, all in the orthorhombic phase.

| Compound | NM | FM | NN-AFM | SDW |
|---|---|---|---|---|
| CaFe$_2$As$_2$ | 2.6 | 2.4 | 2.7 | 3.1 |
| SrFe$_2$As$_2$ | 0.2 | 0.3 | 0.2 | −1.3 |
| BaFe$_2$As$_2$ | −1.1 | −1.0 | −1.3 | +1.3 |

The orthorhombic splitting of the axes in the $(a, b)$ plane has a rather small influence on the EFG. The EFG is larger for the orthorhombic symmetry for small Fe–As distances, i.e. $\Delta z < -0.1\,Å$. In the case of SrFe$_2$As$_2$, the effect of the orthorhombic splitting is so small that the orthorhombic EFG curve in figure 11 is not shown (see the middle panel of figure 11). In the case of BaFe$_2$As$_2$, we observe a similar behaviour as for CaFe$_2$As$_2$. The tetragonal and orthorhombic EFG curves cross close to the EFG minimum and the EFG is larger for the orthorhombic symmetry for smaller Fe–As distances, i.e. $\Delta z < +0.1\,Å$. For all the three compounds, we find that $V_{zz}$ is parallel to the crystallographic $z$-axis for the NM calculations in both the tetragonal and orthorhombic symmetry.

Investigation of the influence of magnetism on the EFG in the orthorhombic symmetry shows that FM or NN-AFM ordering of the Fe atoms does not change the EFG much; however, the SDW order has a huge influence on the EFG, cf table 4. For all the three systems, as the Fe–As distance is decreased, the magnetic moment is reduced and finally tends to zero. At this displacement value, the SDW EFG curves smoothly join the NM orthorhombic EFG curves as one would expect. In figure 11 the component of the EFG that is parallel to the $z$-axis of the crystal is shown. As mentioned before, $V_{zz}$ is found to be parallel to the crystallographic $z$-axis in all NM calculations. For the magnetic SDW phase the same behaviour is observed for CaFe$_2$As$_2$, but not for SrFe$_2$As$_2$ and BaFe$_2$As$_2$. For the latter two compounds, $V_{zz}$ changes the axis, i.e. the axis along which EFG is the largest changes as the Fe–As distance is varied. For BaFe$_2$As$_2$, such a behaviour was also observed experimentally [45] when going from the high-temperature NM tetragonal phase to the low-temperature SDW phase. Unfortunately for CaFe$_2$As$_2$, only the quadrupole frequency parallel and not perpendicular to the crystallographic $z$-axis is provided in reference [44]. The three diagonal components of the EFG tensor $V_{ii}$, which are parallel to the $x$-, $y$- and $z$-axes of the crystal, vary continuously as a function of the As $z$ position, as can be seen in figure 12. In the case of SrFe$_2$As$_2$, $V_{zz}$ is parallel to the $x$-axis for a displacement of As between +0.05 and −0.075 Å (which includes the experimental As $z$ position) and parallel to the $z$-axis for a displacement between −0.1 and −0.15 Å. For BaFe$_2$As$_2$, according to its definition as the largest component, $V_{zz}$ fluctuates between all the three different axes (figure 12). In particular, at the experimental As $z$ position, $V_{zz}$ is parallel to the $y$-axis. We also observe that the component parallel to the $x$-axis is very similar for both the Sr and Ba 122 compounds. The components parallel to the $y$- and $z$-axes show the same variation with the As $z$ position, but only the values for the two compounds are shifted by an almost constant amount. Figure 3 in [44] shows the temperature dependence of the quadrupole frequency $\nu_Q$ for CaFe$_2$As$_2$: $\nu_Q$ increases drastically from 300 to 170 K. At 170 K there is a large jump in the frequency due to the orthorhombic SDW phase transition. Between 170 and 20 K, $\nu_Q$ is rather constant. The calculated EFGs correspond to lattice parameters at 250 and 50 K. For these two temperatures the quadrupole frequency (parallel to the crystallographic $z$-axis) is
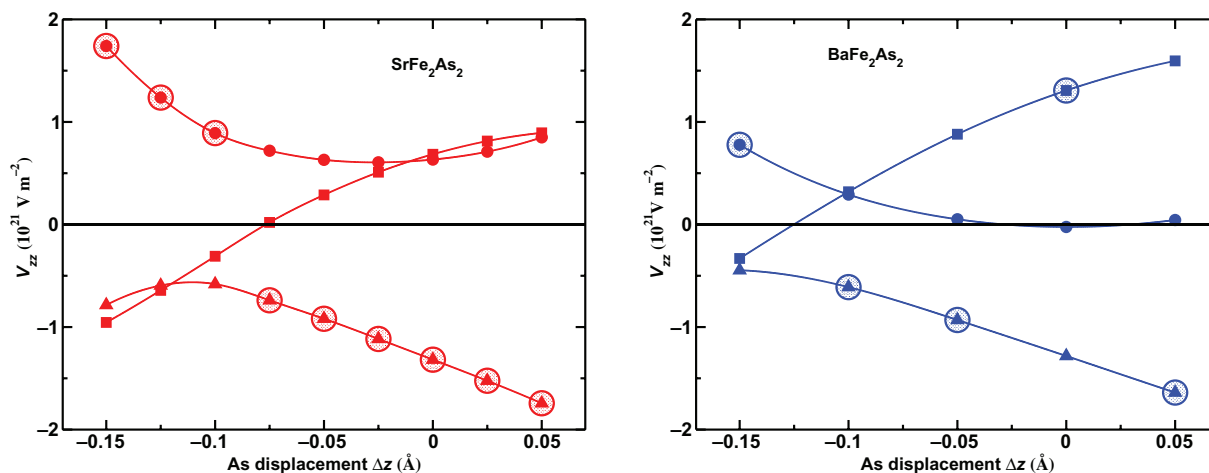
**Figure 12.** Left panel: the three components of the EFG tensor for $SrFe_2As_2$ in the orthorhombic SDW phase as a function of the As $z$ position. $\Delta z = z - z_{exp}$. The component of the EFG parallel to the crystallographic $x$-axis is shown by triangles, the component parallel to the crystallographic $y$-axis by squares and the one parallel to the crystallographic $z$-axis by solid circles. $V_{zz}$, the largest of these three, is marked by a large shaded circle for each As $z$ position. Right panel: the three components of the EFG tensor for $BaFe_2As_2$ in the orthorhombic SDW phase as a function of the As $z$ position. The rest of the notation is the same as that of the left panel.

almost identical. This is in agreement with our result for the experimental As $z$ position as seen in the upper panel of figure 11.

We also investigated the influence of pressure on the EFG. $V_{zz}$ for different pressures was calculated for $CaFe_2As_2$ [45] and $SrFe_2As_2$ [16] using the experimental structural parameters reported as a function of pressure. Our result is shown in the inset of figure 13. In the case of $CaFe_2As_2$, the EFG increases when the applied pressure is increased from 0 to 0.24 GPa. For these pressures the structure is in the (orthorhombic) SDW phase. The next experimental pressure point is larger than the critical pressure of 0.3 GPa (section 3.3), where the $c/a$ collapse takes place. The structure changes into the NM tetragonal phase and the calculated EFG increases drastically from roughly 3 to $10 \times 10^{21}$ V m$^{-2}$. Experimentally, the applied pressure for $SrFe_2As_2$ was much higher (up to 4 GPa) than for $CaFe_2As_2$, but no indications of a collapsed phase has been found till now. Contrary to the jump in the calculated EFG at 0.3 GPa for $CaFe_2As_2$, EFG for $SrFe_2As_2$ increases monotonously without any kinks up to 4 GPa. It is worth measuring the EFG for these systems to get a clearer picture.

Finally, the EFGs of the $A$ site doped compounds were calculated with VCA. The validity of the VCA was checked by supercell calculations for $SrFe_2As_2$ and $BaFe_2As_2$. Due to the supercell construction, there are three different Wyckoff positions for As and hence three different EFGs, which lie reasonably close to the VCA EFG curve. In the VCA calculation we keep the structural parameters fixed for the different levels of doping. In figure 13 EFGs calculated in this manner are shown for $CaFe_2As_2$, $SrFe_2As_2$ and $BaFe_2As_2$. In the case of $CaFe_2As_2$, the EFG increases when electrons are taken out and decreases when electrons are added to the system. This implies that the As electron density gets more isotropic when the
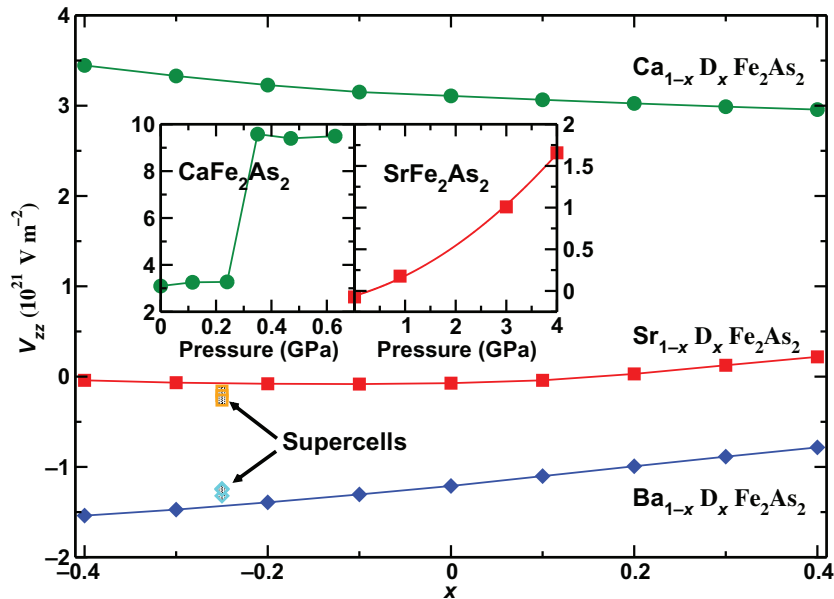
**Figure 13.** EFGs calculated for doped $CaFe_2As_2$ (green circles), $SrFe_2As_2$ (red squares) and $BaFe_2As_2$ (blue diamonds) using VCA. Results obtained from a fourfold supercell for $x = -0.25$ for $SrFe_2As_2$ (shaded orange squares) and $BaFe_2As_2$ (shaded blue diamonds) in the NM tetragonal phase are also shown. Inset: dependence of the EFG on pressure for $CaFe_2As_2$ (left) and $SrFe_2As_2$ (right). The latter is in the (NM) tetragonal phase.

system is electron doped. For $BaFe_2As_2$, the trend is the same as in $CaFe_2As_2$, whereas for $SrFe_2As_2$ the situation is slightly different: hole doping does not change the EFG much, whereas electron doping increases the EFG. Note, however, that the calculated EFG for $SrFe_2As_2$ is quite small.

We conclude that the EFG in the 122 and in the 1111 systems behave similarly [47, 48]: the effect of electron doping on the EFG is much smaller than the influence of the As $z$ position and pressure (compare figures 11 and 13). This finding emphasizes again the crucial importance of a correct description of the Fe–As interaction (which is mostly responsible for the density around As) for a better understanding of the physical properties of the iron pnictides.

## 4. Results—experiment

### 4.1. Substitutions of Fe by other 3d-metals

As already mentioned, at ambient pressure, no bulk superconductivity has been observed in stoichiometric $RE$OFeAs and $A$Fe$_2$As$_2$ ($A =$ Ca, Sr, Ba, Eu) compositions (except for one report on $SrFe_2As_2$ crystals [49]). Instead, these parent compounds display the SDW transition at typically 100–200 K. A modification of the intralayer $d_a^{Fe-Fe}$ and interlayer $d_c^{Fe-Fe}$ distances and thus of the electronic states at $E_F$ can be achieved by different means: (i) application of hydrostatic (or uniaxial) pressure, (ii) isovalent substitution of a constituent atom by a smaller/larger ion in order to apply chemical pressure, (iii) hole doping or (iv) electron doping by non-isovalent substitution of any of the constituent atoms. The latter two methods usually also

exert chemical pressure. Most excitingly, all these methods have been proved to be successful in generating bulk superconductivity in iron arsenide systems.

Application of pressure has widely been used to explore the phase diagrams of the superconducting chemical systems [38, 40, 50]. The method usually introduces no crystallographic disorder in the structural building units. In contrast, when substituting a chemical constituent (methods (ii)–(iv)) always a certain degree of structural disorder is introduced. First, only substitutions on sites *in-between the Fe–As layers* were attempted. Based on the experience gained from extensive work on cuprates, such an indirect doping of the Fe–As layers is expected to introduce only minor structural disorder. In a localized (cuprate-like) as well as in an itinerant model of the arsenides, this type of doping amounts to a simple charge doping. Such experiments are therefore not suitable for discriminating between both models.

In contrast, the substitution of an atom species *within the Fe–As layer* can yield more information on the underlying physics. In an itinerant model the substitution of a small amount of Fe by another d element (*TM*) is expected to be similar to indirect doping since only the total count of electrons is relevant, i.e. a rigid-band picture should work in first approximation. In a picture with localized d electrons, on the other hand, doping on the Fe site should directly affect the correlations in the Fe–As layers. A behaviour drastically different from indirect doping should evolve. In cuprates the substitution of a few percent Ni or Zn on the Cu site leads to a strong reduction of $T_c$.

Therefore, several groups recently investigated the properties of solid solutions of the type $RE$O(Fe$_{1-x}$Co$_x$)As or $A$Fe$_{2-x}$Co$_x$As$_2$. Sefat *et al* [51] and Wang *et al* [52] first reported superconductivity in cobalt doped LaOFeAs with a maximum $T_c$ of $\approx 10$ K. Our group concentrated on the system SrFe$_{2-x}TM_x$As$_2$: while the pure Fe compound undergoes a lattice distortion and SDW ordering at $T_0 = 205$ K [10], Co substitution leads to a rapid decrease in $T_0$, followed by the onset of bulk superconductivity in the concentration range $0.2 \leqslant x \leqslant 0.4$ [14]. The maximum $T_c$ of $\approx 20$ K is achieved for $x \approx 0.20$. This was in fact also the first observation of *electron-doping* induced superconductivity in $A$Fe$_2$As$_2$ compounds. Co substitution also generated bulk superconductivity with the maximum $T_c$ of $\approx 22$ K in BaFe$_{2-x}$Co$_x$As$_2$ [15]; however, the optimal doping seems to be lower than in the Sr system [53]. Substitution of the following *TM*, nickel, introducing twice as many electrons per atom into the Fe–As layer, also generates bulk superconductivity, albeit with lower $T_c$ than Co substitution in the Sr compound [14]. However, for the corresponding Ba compound, $T_c$ up to 21 K is reported for BaFe$_{1.90}$Ni$_{0.10}$As$_2$ [54]. Only very recently, another internal substitution, namely of As by P, was reported for EuFe$_2$As$_2$ [55] and LaOFeAs [56]. Also by this means the SDW transition can be influenced and superconductivity can be induced.

In table 5, we present the lattice parameters and the SDW and superconducting transition temperatures ($T_0$, $T_c$) of several SrFe$_{2-x}TM_x$As$_2$ solid solutions. Values for $T_0$ can be most easily obtained from the corresponding anomaly in resistivity data (see figure 14). Besides Co and Ni substitutions in the Sr122 and Ba122 systems, no further d element substitutions have been reported yet. As demonstrated recently [14], substitution of Fe by Co suppresses rapidly $T_0$ (see figure 14). Bulk superconductivity, as proved by specific heat, magnetic shielding and resistivity data, appears when $T_0 = 0$ or $T_0 < T_c$, which is reached for $x > 0.20$ [14]. Only about half of the substituting element ($x \approx 0.10$) is necessary to induce bulk superconductivity when using nickel [54]. Both elements then introduce 0.2 excess electrons into the FeAs layers. While the $a$ lattice parameter does not change significantly with Co substitution, the $c$ lattice parameter decreases continuously in SrFe$_{2-x}$Co$_x$As$_2$ [14] and with Ni content in BaFe$_{2-x}$Ni$_x$As$_2$ [54].

**Table 5.** Lattice parameters $a$ and $c$ of some $SrFe_{2-x}TM_xAs_2$ (nominal compositions) phases and superconducting transition temperature $T_c^{mag}$ from magnetization measurements (onset, $T_{min} = 1.8$ K).

| TM | $x$ | $a$ (Å) | $c$ (Å) | $T_c^{mag}$ (K) | $T_0$ (K) | Reference |
|----|-----|---------|---------|-----------------|-----------|-----------|
| –  | 0.00 | 3.924(3) | 12.38(1) | – | 205 | [10] |
| Co | 0.10 | 3.9291(1) | 12.3321(7) | – | 130 | [14] |
|    | 0.15 | 3.9272(1) | 12.3123(5) | – | 90 | [14] |
|    | 0.20 | 3.9278(2) | 12.3026(2) | 19.2 | <30 | [14] |
|    | 0.25 | 3.9296(2) | 12.2925(9) | 18.1 | – | [14] |
|    | 0.30 | 3.9291(2) | 12.2704(8) | 13.2 | – | [14] |
|    | 0.40 | 3.9293(1) | 12.2711(7) | 12.9 | – | [14] |
|    | 0.50 | 3.9287(2) | 12.2187(9) | – | – | [14] |
|    | 2.00 | 3.9618(1) | 11.6378(6) | – | – | [14] |
| Ni | 0.10 | 3.9299(1) | 12.3238(6) | ≈8 | <85 | [14] |
| Mn | 0.10 | 3.9319(2) | 12.4161(7) | – | 165 | This work |
|    | 0.20 | 3.9384(3) | 12.4615(23) | – | 130 | This work |
|    | 0.30 | 3.9441(2) | 12.4832(7) | – | 130 | This work |
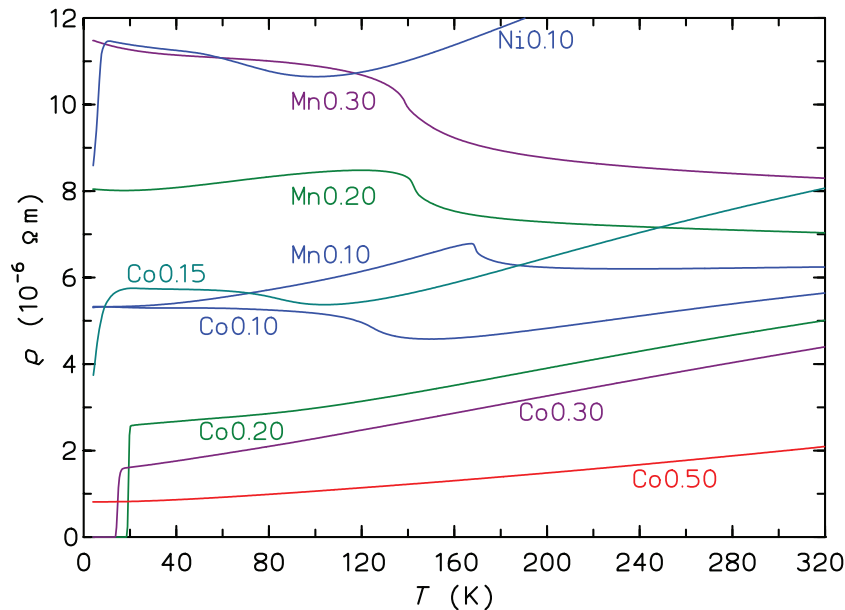


**Figure 14.** Electrical resistivity of polycrystalline $SrFe_{2-x}TM_xAs_2$ ($TM$ = Mn, Co or Ni) samples.

Chemical homogeneity of the Co or Ni distribution is still an issue in current samples. One of the most important questions, the co-existence or mutual exclusion of the SDW state and bulk superconductivity, has been discussed heavily for the $AFe_2As_2$-based alloy series [57]–[59]. The answer is currently open and can be given only for really homogeneous samples.

Direct, in-plane *hole* doping might also induce superconductivity. Our new investigations show that the substitution of Fe by Mn is possible and that it leads to a continuous increase of both the $a$ and $c$ lattice parameters with Mn content. Under these conditions, a hole doping does not generate superconductivity. In contrast, in the indirectly doped $Sr_{1-x}K_xFe_2As_2$ [3, 60] and $Ba_{1-x}K_xFe_2As_2$ [5] compounds, the $a$ lattice parameter decreases with $x$, whereas $c$ increases, keeping the unit cell volume almost constant. Also, the SDW transition temperature $T_0$ is suppressed with increasing Mn content in a different way (see figure 14) than for the Co and Ni substitutions where $T_0$ is suppressed for $x \approx 0.20$ and $x \approx 0.10$, respectively. Indeed, after an initial decrease of $T_0$ to $\approx 140$ K for $x = 0.20$, the transition temperature seems to not decrease further with $x$. Thus, the doping with holes or electrons is not the only important factor for the appearance of superconductivity but a corresponding tuning of the distances $d_a^{Fe-Fe}$ and $d_c^{Fe-Fe}$ has to be also accomplished. At present, the microscopic origin of the differences upon Mn doping compared with Co or Ni doping is unclear. Therefore, further investigations for different substitutions are currently under way.

Magnetic susceptibility and specific heat data for polycrystalline samples $SrFe_{2-x}Co_xAs_2$ have already been presented [14]. Here, instead we report newer data obtained on two crystals with Co contents $x > 0.2$ that were grown by a flux method (see section 2.2).

Both crystals show strong diamagnetic signals in measurements after zero-field cooling (ZFC). The onset temperatures $T_c^{mag}$ are 17.8 and 15.3 K, respectively. While the transition for crystal X1 is much wider than that of crystal X2, the $T_c$ of the latter is somewhat lower, indicating a slightly larger Co content in accordance with the EPMA investigations. The shielding signals (ZFC) correspond to the whole sample volume; however, the Meissner effect (FC) is very small. This is typical for Co-substituted $AFe_2As_2$ materials and is probably due to strong flux line pinning. The random (and somewhat inhomogeneous) substitution of Fe by Co within the superconducting layers seems to introduce effective pinning centres. This is a remarkable difference from superconducting compositions with substitutions outside the Fe–As layers.

As has already been demonstrated [14], the SDW ordering and the connected lattice distortion at $T_0 = 205$ K in $SrFe_2As_2$ [10, 27] are strongly suppressed by Co substitution, similarly to K substitution (indirect hole doping) [60]. For the two crystals, no corresponding anomaly in $\rho(T)$ is observed.

The specific heat $c_p(T)$ for the two crystals is shown in figure 15 in a $c_p/T$ versus $T^2$ representation. It can be clearly seen that crystal X1 has a very broad transition (with a 'foot' at the high-temperature side), whereas crystal X2 displays a rounded but single-step anomaly. The specific heat jumps $\Delta c_p/T_c$ and the transition temperatures $T_c^{cal}$ can be evaluated by a fit including a phonon background (harmonic lattice approximation) and an electronic term $c_{es}(T)$ according to the Bardeen–Cooper–Schrieffer (BCS) theory ($\Delta c_p/T_c = 1.43\gamma$) or the phenomenological two-liquid model ($\Delta c_p/T_c = 2\gamma$, a model for stronger e–ph coupling). The inclusion of a residual linear term $\gamma'T$ was found to be absolutely necessary for a good fit:

$$c_p(T) = \gamma'T + \beta T^3 + \delta T^5 + c_{es}(T).$$

The jump at $T_c$ is 'broadened' in order to simulate the rounding of the transition steps due to chemical inhomogeneities. For the more homogeneous sample X2 no difference in the least-squares deviation is observed between the BCS theory and the two-fluid model. We find for crystal X2 $\Delta c_p/T_c^{cal} \approx 12.0$ mJ mol$^{-1}$ K$^{-2}$ at $T_c^{cal} = 12.34$ K and also for crystal X1 similar
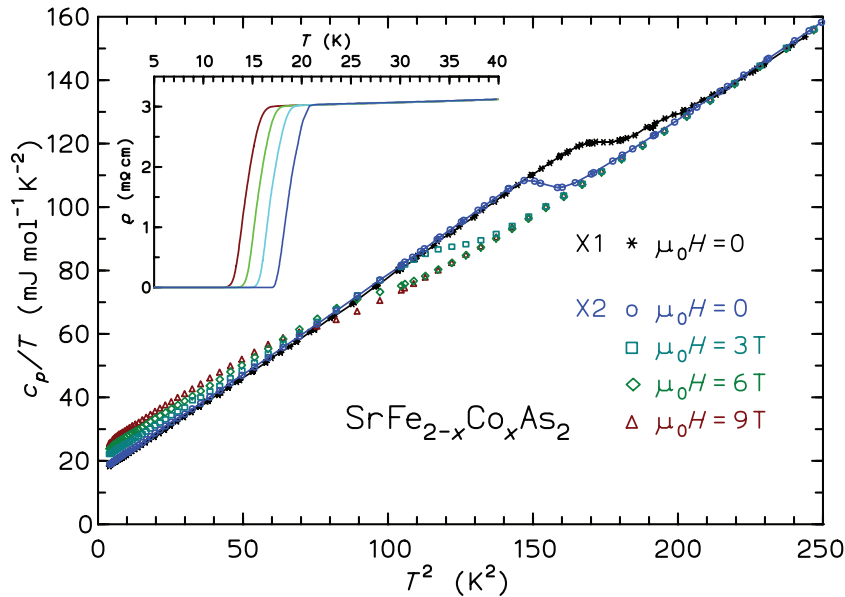
**Figure 15.** Molar isobaric specific heat $c_p/T^2$ of $SrFe_{2-x}Co_xAs_2$ crystal samples for different magnetic fields. For crystal X1, only data for $\mu_0 H = 0$ are given. Zero-field data points are connected by a line. The inset shows the resistivity of crystal X2 around $T_c$ for $\mu_0 H = 0.01, 3, 6$ and $9$ T.

values ($\approx 12.5\,\mathrm{mJ\,mol^{-1}K^{-2}}$; $T_c = 13.22$ K). Similar values of $\Delta c_p / T_c^{\mathrm{cal}}$ were observed in our previous study [14] of polycrystalline samples with Co contents $x = 0.20$ and $0.30$.

The existence of a linear specific heat term well below $T_c$ is found for several $A\mathrm{Fe_2As_2}$-based alloys [14, 61]. For $H = 0$, we observe, for both crystals, values of $\gamma'$ around $20\,\mathrm{mJ\,mol^{-1}\,K^{-2}}$. $\gamma'$ generally increases with field. Whether the residual $\gamma'$ is due to defects as in the case of early cuprate superconductor samples (see e.g. [62]) or whether it is an intrinsic contribution has to be clarified by further experiments. An intrinsic reason could be some ungapped parts of the Fermi surface [63]. For the specific heat jump $\Delta c_p / T_c$ in $\mathrm{BaFe_{2-x}Co_xAs_2}$ also relatively small values are reported ($\approx 25\,\mathrm{mJ\,mol^{-1}\,K^{-2}}$ [53]), whereas for $\mathrm{Ba_{0.6}K_{0.4}Fe_2As_2}$ ($\Delta c_p / T_c \approx 100\,\mathrm{mJ\,mol^{-1}\,K^{-2}}$ [57, 61]) much larger jumps are observed. This may indicate that the superconducting Fermi surface portions in the Co-substituted compounds (in-plane doping) are strongly different from those in indirectly doped superconductors. Recent angle-resolved photoemission spectroscopy (ARPES) investigations indeed point out severe differences between (non-superconducting) $\mathrm{BaFe_{1.7}Co_{0.3}As_2}$ and (superconducting) $\mathrm{Ba_{0.6}K_{0.4}Fe_2As_2}$ [64]. In conclusion, our doping experiments on the Fe site strongly favour an itinerant picture over a localized scenario. Further thermodynamic and Fermi surface studies are required to resolve this issue.

## 5. Summary

In this paper, we presented a joint theoretical and experimental study of the systems $A\mathrm{Fe_2As_2}$ ($A = $ Ca, Sr, Ba, Eu) and $\mathrm{SrFe_{2-x}}TM_x\mathrm{As_2}$ ($TM = $ Mn, Co, Ni) to investigate the relation of crystal structure and charge doping to magnetism and superconductivity in these compounds.

Based on *ab initio* electronic structure calculations we focused on the relationship between the crystal and electronic structure, charge doping and magnetism for the 122 family since their electronic structure and physical properties are quite similar to the other superconducting iron pnictide families (1111, 1111′, 111, 11).

Although problems in regard to an accurate description of the Fe–As interaction persist in present-day density functional calculations, this approach provides deep insights into many questions. We demonstrate that the tetragonal to orthorhombic transition in the 122 compounds is intrinsically linked to the SDW formation in agreement with experimental observations. We find an anisotropic, pressure-induced volume collapse for $A\text{Fe}_2\text{As}_2$ ($A = $ Ca, Sr, Ba, Eu) that goes along with the suppression of the SDW magnetic order. For $A = $ Ca our calculations are in excellent agreement with the experimental observations [25]. An experimental verification for the other compounds ($A = $ Sr, Ba, Eu) would be desirable. With respect to the doping dependence in $\text{SrFe}_{2-x}\,TM_x\text{As}_2$, we find the correct trends compared with the experimental results. A more quantitative comparison will require the explicit treatment of the influence of the substitutional disorder on electronic structure and magnetism. This task is left for an extended future study.

As demonstrated also for the EFG, many properties of these compounds are sensitive to the As $z$ position. Since the magnetism and therefore the superconductivity crucially depend on this structural feature and the related accurate description of the Fe–As interaction, the improvement of the calculations in this respect may offer the key to the understanding of superconductivity in the whole family. In order to improve the present-day density functional calculation for this class of materials, the first step requires a deeper understanding of where, how and why these DFT calculations fail. Besides further calculational effort, a broader experimental basis, especially high-pressure studies, will be necessary to approach this complex issue.

Experimentally, we investigate the substitution of Fe in $\text{SrFe}_{2-x}TM_x\text{As}_2$ by other 3d transition metals, $TM = $ Mn, Co, Ni. In contrast to a partial substitution of Fe by Co or Ni (electron doping), a corresponding Mn partial substitution does not lead to the suppression of the AFM order or the appearance of superconductivity.

The observed existence of a linear specific heat term in $\text{SrFe}_{2-x}\text{Co}_x\text{As}_2$ well below $T_c$ is extremely important for the understanding of the superconductivity not only in this compound but also in all related 122 superconductors with doping on the Fe site. Therefore, a careful investigation of the question of whether this feature is intrinsic or not is crucial. In order to answer it, further studies on carefully prepared and characterized high-quality samples are required. Since in many experiments a considerable sample dependence is observed, this issue is of high general importance for the understanding in future of the superconducting iron pnictide materials.

## Acknowledgments

## References

[1] Kamihara Y, Watanabe T, Hirano M and Hosono H 2008 *J. Am. Chem. Soc.* **130** 3296–7
[2] Ren Z A *et al* 2008 *Chin. Phys. Lett.* **25** 2215

[3] Sasmal K, Lv B, Lorenz B, Guloy A M, Chen F, Xue Y and Chu C 2008 *Phys. Rev. Lett.* **101** 107007

[4] Chen G F, Li Z, Li G, Hu W Z, Dong J, Zhang X D, Zheng P, Wang N L and Luo J L 2008 *Chin. Phys. Lett.* **25** 3403

[5] Rotter M, Tegel M and Johrendt D 2008 *Phys. Rev. Lett.* **101** 107006

[6] Wang X C, Liu Q Q, Lv Y X, Gao W B, Yang L X, Yu R C, Li F Y and Jin C Q 2008 arXiv:0806.4688v3

[7] Mizuguchi Y, Tomioka F, Tsuda S, Yamaguchi T and Takano Y 2008 *Appl. Phys. Lett.* **93** 152505

[8] Wu G *et al* 2008 arXiv:0811.0761v2

[9] Ronning F, Klimczuk T, Bauer E D, Volz H and Thompson J D 2008 *J. Phys.: Condens. Matter* **20** 322201

[10] Krellner C, Caroca-Canales N, Jesche A, Rosner H, Ormeci A and Geibel C 2008 *Phys. Rev.* B **78** 100504

[11] Rotter M, Tegel M, Schellenberg I, Hermes W, Pöttgen R and Johrendt D 2008 *Phys. Rev.* B **78** 020503

[12] Jeevan H S, Hossain Z, Kasinathan D, Rosner H, Geibel C and Gegenwart P 2008 *Phys. Rev.* B **78** 052501

[13] Jeevan H S, Hossain Z, Kasinathan D, Rosner H, Geibel C and Gegenwart P 2008 *Phys. Rev.* B **78** 092406

[14] Leithe-Jasper A, Schnelle W, Geibel C and Rosner H 2008 *Phys. Rev. Lett.* **101** 207004

[15] Sefat A S, Jin R, McGuire M A, Sales B C, Singh D J and Mandrus D 2008 *Phys. Rev. Lett.* **101** 117004

[16] Kumar M, Nicklas M, Jesche A, Caroca-Canales N, Schmitt M, Hanfland M, Kasinathan D, Schwarz U, Rosner H and Geibel C 2008 *Phys. Rev.* B **78** 184516

[17] Koepernik K and Eschrig H 1999 *Phys. Rev.* B **59** 1743

[18] Opahle I, Koepernik K and Eschrig H 1999 *Phys. Rev.* B **60** 14035

[19] Perdew J P and Wang Y 1992 *Phys. Rev.* B **45** 13244

[20] Czyżyk M T and Sawatzky G A 1994 *Phys. Rev.* B **49** 14211

[21] Anisimov V I, Zaanen J and Andersen O K 1991 *Phys. Rev.* B **44** 943

[22] Liechtenstein A I, Anisimove V I and Zaanen J 1995 *Phys. Rev.* B **52** R5467

[23] Morinaga R, Matan K, Suzuki H S and Sato T J 2008 arXiv:0809.3084v2

[24] Bostrom M, Prots Y and Grin Y 2006 *J. Solid State Chem.* **179** 2472

[25] Kreyssig A *et al* 2008 *Phys. Rev.* B **78** 184517

[26] Jesche A *et al* 2008 *Phys. Rev.* B **78** 180504

[27] Tegel M, Rotter M, Weiss V, Schappacher F M, Pöttgen R and Johrendt D 2008 *J. Phys.: Condens. Matter* **20** 452201

[28] Ma C, Yang H, Tian H, Shi H, Lu J, Wang Z, Zeng L, Chen G, Wang N and Li J 2008 arXiv:0811.3270v2

[29] Huang Q, Qiu Y, Bao W, Lynn J, Green M, Chen Y, Wu T, Wu G and Chen X 2008 *Phys. Rev. Lett.* **101** 257003

[30] Wu G, Chen H, Wu T, Xie Y L, Yan Y J, Liu R H, Wang X F, Ying J J and Chen X H 2008 *J. Phys.: Condens. Matter* **20** 422201

[31] Mazin I I, Johannes M D, Boeri L, Koepernik K and Singh D J 2008 *Phys. Rev.* B **78** 085104

[32] Mazin I I and Johannes M D 2008 arXiv:0807.3737v1

[33] Goko T *et al* 2008 arXiv:0808.1425v1

[34] Goldman A I *et al* 2008 *Phys. Rev.* B **78** 100506

[35] Zhao J *et al* 2008 *Phys. Rev.* B **78** 140504

[36] Matan K, Morinaga R, Iida K and Sato T J 2008 arXiv:0810.4790

[37] Yildirim T 2008 arXiv:0807.3936v2

[38] Torikachvili M S, Bud'ko S L, Ni N and Canfield P C 2008 *Phys. Rev. Lett.* **101** 057006

[39] Miclea C F, Nicklas M, Jeevan H S, Kasinathan D, Hossain Z, Rosner H, Gegenwart P, Geibel C and Steglich F 2008 arXiv:0808.2026v1

[40] Alireza P L, Ko Y T C, Gillett J, Petrone C M, Cole J M, Lonzarich G G and Sebastian S E 2008 *J. Phys.: Condens. Matter* **21** 012208

[41] Yu W, Aczel A A, Williams T J, Bud'ko S L, Ni N, Canfield P C and Luke G M 2008 arXiv:0811.2554v1

[42] Pyykkö P 2001 *Mol. Phys.* **99** 1617

[43] Abragam A 2006 *The Principles of Nuclear Magnetism* (Oxford: Oxford University Press)

[44] Baek S H, Curro N J, Klimczuk T, Bauer E D, Ronning F and Thompson J D 2008 arXiv:0808.0744v3

[45] Kitagawa K, Katayama N, Ohgushi K, Yoshida M and Takigawa M 2008 arXiv:0807.4613v3
[46] Jeglič P 2008 private communication
[47] Grafe H J *et al* 2008 arXiv:0811.4508
[48] Jeglič P, Bos J W G, Zorko A, Brunelli M, Koch K, Rosner H, Margadonna S and Arčon D 2008 *Phys. Rev. B* at press
[49] Saha S R, Butch N P, Kirshenbaum K and Paglione J 2008 arXiv:0811.3940v1
[50] Park T, Park E, Lee H, Klimczuk T, Bauer E D, Ronning F and Thompson J D 2008 *J. Phys.: Condens. Matter* **20** 322204
[51] Sefat A S *et al* 2008 *Phys. Rev.* B **78** 104505
[52] Cao G *et al* 2008 arXiv:0807.1304v2
[53] Tanatar M A, Ni N, Martin C, Gordon R T, Kim H, Kogan V G, Samolyuk G D, Bud'ko S L, Canfield P C and Prozorov R 2008 arXiv:0808.4991v1
[54] Li L J *et al* 2008 arXiv:0809.2009v1
[55] Ren Z, Tao Q, Jiang S, Feng C, Wang C, Dai J, Cao G and Xu Z 2008 arXiv:0811.2390v1
[56] Wang C, Jiang S, Tao Q, Ren Z, Li Y, Li L, Feng C, Dai J and abd Zhu'an Xu G C 2008 arXiv:0811.3925v1
[57] Rotter M, Tegel M, Schellenberg I, Schappacher F M, Pöttgen R, Deisenhofer J, Günther A, Schrettle F, Loidl A and Johrendt D 2008 arXiv:0812.2827v1
[58] Chu J, Analytis J G, Kucharczyk C and Fisher I R 2008 arXiv:0811.2463v1
[59] Wang X F, Wu T, Wu G, Liu R H, Chen H, Xie Y L and Chen X H 2008 arXiv:0811.2920v1
[60] Chen G F *et al* 2008 *Chin. Phys. Lett.* **25** 3403
[61] Mu G, Luo H, Wang Z, Ren Z, Shan L, Ren C and Wen H 2008 arXiv:0812.1188v1
[62] Triscone G and Junod A 1996 *Bismuth-Based High-Temperature Superconductors* ed H Maeda and K Togano (New York: Marcel Dekker) pp 33–74
[63] Drechsler S L *et al* 2003 *Physica* B **329** 1352–4
[64] Sekiba Y *et al* 2008 arXiv:0812.4111v1